Check for updates

Tuneable hydrogel patterns in pillarless microfluidic devices†

Claudia Olaizola-Rodrigo, [iD] [ad] Sujey Palma-Florez, [iD] [ef] Teodora Ranđelović, [iD] [abc] Clara Bayona, [iD] [ab] Mehran Ashrafi, [iD] [a] Josep Samitier, [iD] [cef] Anna Lagunas, [iD] [ce] Mònica Mir, [iD] [cef] Manuel Doblaré, [iD] [abc] Ignacio Ochoa, [iD] *[abc] Rosa Monge [iD] *[d] and Sara Oliván [iD] *[ab]

Organ-on-chip (OOC) technology has recently emerged as a powerful tool to mimic physiological or pathophysiological conditions through cell culture in microfluidic devices. One of its main goals is bypassing animal testing and encouraging more personalized medicine. The recent incorporation of hydrogels as 3D scaffolds into microfluidic devices has changed biomedical research since they provide a biomimetic extracellular matrix to recreate tissue architectures. However, this technology presents some drawbacks such as the necessity for physical structures as pillars to confine these hydrogels, as well as the difficulty in reaching different shapes and patterns to create convoluted gradients or more realistic biological structures. In addition, pillars can also interfere with the fluid flow, altering the local shear forces and, therefore, modifying the mechanical environment in the OOC model. In this work, we present a methodology based on a plasma surface treatment that allows building cell culture chambers with abutment-free patterns capable of producing precise shear stress distributions. Therefore, pillarless devices with arbitrary geometries are needed to obtain more versatile, reliable, and biomimetic experimental models. Through computational simulation studies, these shear stress changes are demonstrated in different designed and fabricated geometries. To prove the versatility of this new technique, a blood–brain barrier model has been recreated, achieving an uninterrupted endothelial barrier that emulates part of the neurovascular network of the brain. Finally, we developed a new technology that could avoid the limitations mentioned above, allowing the development of biomimetic OOC models with complex and adaptable geometries, with cell-to-cell contact if required, and where fluid flow and shear stress conditions could be controlled.

1. Introduction

Since their appearance in the last decade of the 20th century, microfluidic devices have transformed several fields of science and technology with applications ranging from optics to drug discovery, point-of-care clinical diagnostics, sensors and bioanalytical systems and other areas in biomedicine.

[a] *Tissue Microenvironment (TME), Lab. Aragón Institute of Engineering Research (I3A), University of Zaragoza, Zaragoza, Spain. E-mail: iochgar@unizar.es, soligar@unizar.es*

[b] *Institute for Health Research Aragón (IIS Aragón), Zaragoza, Spain*

[c] *CIBER-BBN, ISCIII, Spain*

[d] *BEOnChip S.L., Zaragoza, Spain. E-mail: rmonge@beonchip.es*

[e] *Nanobioengineering Group, Institute for Bioengineering of Catalonia (IBEC), Barcelona Institute of Science and Technology (BIST), Spain*

[f] *Department of Electronics and Biomedical Engineering, University of Barcelona, Martí i Franquès 1, 08028 Barcelona, Spain*

† Electronic supplementary information (ESI) available. See DOI: https://doi.org/10.1039/d3lc01082a

One of these topics is no doubt OOC systems.[1] An organ-on-chip is a miniature micro-engineering system that combines biomaterials technology, cell biology and engineering to reproduce the structural and functional attributes of human tissue on a small-scale platform.[2–4]

Microtechnologies permit the fabrication of cell culture chambers and provision and removal of nutrients and gases with micrometer precision, driving to the simulation of controlled biological environments where biological fluid continuously enters slowly but steadily, thus simulating the physiology of organs and tissues.[5] These devices, known as OOC systems, allow mimicking tissue and organ functions, controlling physicochemical microenvironments and reproducing highly accurate tissue interfaces at a level that is not possible for 2D or 3D traditional culture systems. They also enable high-resolution real-time imaging and *in vitro* analysis of biochemical, genetic, and metabolic activities of living cells in a functional pseudo-organ context. This technology has enormous potential to produce disruptive

advances in the study of tissue development, organ physiology, and disease etiology.[4,6–8]

Over the past years, engineered chemical gradients in OOC systems have attracted extensive attention in biomedical applications. Gradients play an essential role in many biological activities and regulate several cellular functions *in vivo*. These gradients of ions, oxygen, and proteins are constantly forming and dissipating within tissues.[9–13] Gradients are also important in the physiological response to injury and diseases by immune cells.[14–16] As a matter of fact, without these biological gradients, many cell functions could not be performed, and complex organisms would not develop. Moreover, chemical gradients affect diverse cellular behaviors such as migration, proliferation, differentiation, inflammation, or tumor evolution.[17–21] For example, oxygen gradients are also related to cell growth, survival, and migration.[22–24] Thus, producing controlled gradients in OOC systems is essential to obtain biomimetic environments and to evaluate those cellular processes in the OOC technology.[25,26]

Gradient devices made of different materials can be found in the literature, but most of the chips are based on micropillars[27–31] to retain the hydrogel inside the chambers. However, these pillars create a physical barrier between the central chamber and the side channels, changing completely the gradient profile, especially close to the pillars. In addition, pillars also hinder direct cell-to-cell contact in co-culture models, which is relevant for some cell types, such as endothelia or epithelia, to the formation of tight junctions between cells to reach a functional barrier.[32] Furthermore, cells can be retained in the pillars avoiding contact with other cells. Finally, pillars alter the shear stress distribution around them, which is especially critical in some applications, since it may change the cell behaviour of certain cell types, avoiding the possibility of getting realistic biomimetic models. To solve these drawbacks, some pillarless devices have been described in the literature. One of the technologies developed is the technique of parallel geometries. However, it was limited to parallel geometries where the shear stress is close to being uniform along the chip; this means that the limitation in terms of designs is high, as the geometries can only be created from three streams running in parallel.[33–36] Another pillar free design is the phaseguide technology which consists of meniscus pinning barriers,[37–39] but this technique does not allow the possibility of designing any geometry. Photopatternable hydrogels,[40–43] although representing a cutting-edge technology, present a challenge due to the complex development and manipulation required, despite their capability to achieve highly varied designs and geometries.

In this work, we developed a microfabrication technique that allows the creation of different geometries and, thus, different shear stress distributions on the hydrogel boundary. This technology is based on a plasma surface treatment that is carried out with the geometry of the desired designs, as there is no limitation in terms of geometry.

To validate the biological feasibility of the chip, a blood–brain barrier model (BBB-on-a-chip) was developed. The BBB is a highly selective barrier that ensures the supply of oxygen and nutrients, avoiding the entry of pathogens or potentially harmful molecules and limiting the access of therapeutic molecules to the central nervous system (CNS).[44] Due to the importance of achieving new therapies for central nervous diseases, the development of a functional BBB model is crucial. In this sense, the design of pillarless microdevices allows the formation of a continuous endothelium, in direct contact with human astrocytes and pericytes, thus helping the formation of the tight junctions (TJs) required for maintaining the restricted BBB permeability.

In summary, a new microfluidic fabrication process for pillarless thermoplastic chips is presented, as well as its validation in a relevant biological setting. This fabrication approach allows obtaining a wide range of geometries with variable and controlled shear stress distribution by creating a diffusion profile uninterrupted by the presence of pillars.

2. Materials and methods

2.1 Microfluidic device fabrication

The device consists of an assembly of thermoplastic materials based on cyclic olefin polymers (COPs) or cyclic olefin copolymers (COCs). The top of the device is an injection molded piece of COP (ZEONOR 1420R) that contains the inlets and outlets of the device where universal screw connectors (1/4-28) can be inserted. The intermediate layer, which contains the channels, is a composite material bonded during the manufacturing process composed of COC Flex (TEKNIFLEX® COC 100 E) and COC Hybrid (TEKNIFLEX® 2203181), and the base of the device, the bottom sheet, is made of a COP (ZEONOR 1420R film) (Fig. 1A and B).

First, the microfluidic device was designed using two software codes: AutoCAD to design the 2D pattern and Solid Edge to establish the 3D model (Fig. 1A). Fig. S1† shows the SolidEdge views of the device. As mentioned above, the device consists of an injection molded part, with the channels defining the chip and the base. The pattern of the channels was done in 2D, and the channels of the final device were designed with the following dimensions: side channels of 0.8 mm in width, 3 mm wide and 4 mm long central chamber, and 1 mm central channel (Fig. 1A). The materials were cut using the 2D patterning process with a plotter (FC8600-60 Wide Vinyl Cutter, Graphtec), and the surface treatment was carried out, consisting of surface activation exposing the materials to oxygen plasma (0.4 mbar, 100 W (50%), 30 s), on the top and the base. For this purpose, an Atto plasma cleaner from Diener electronic was used. Finally, all the components were joined in two steps using a hot embosser (Digital Combo Heat Press, Geo Knight): firstly, the base was bonded to the channels, and then this assembly was bonded to the injection piece (Fig. 1D).

A magnifying lens (Nikon SMZ745) and a confocal microscope (Nikon Eclipse Ti) were used to check the measurements of the device to assess the reproducibility of the fabrication technique. For this purpose, the chamber width, the central channel width, and the height of the
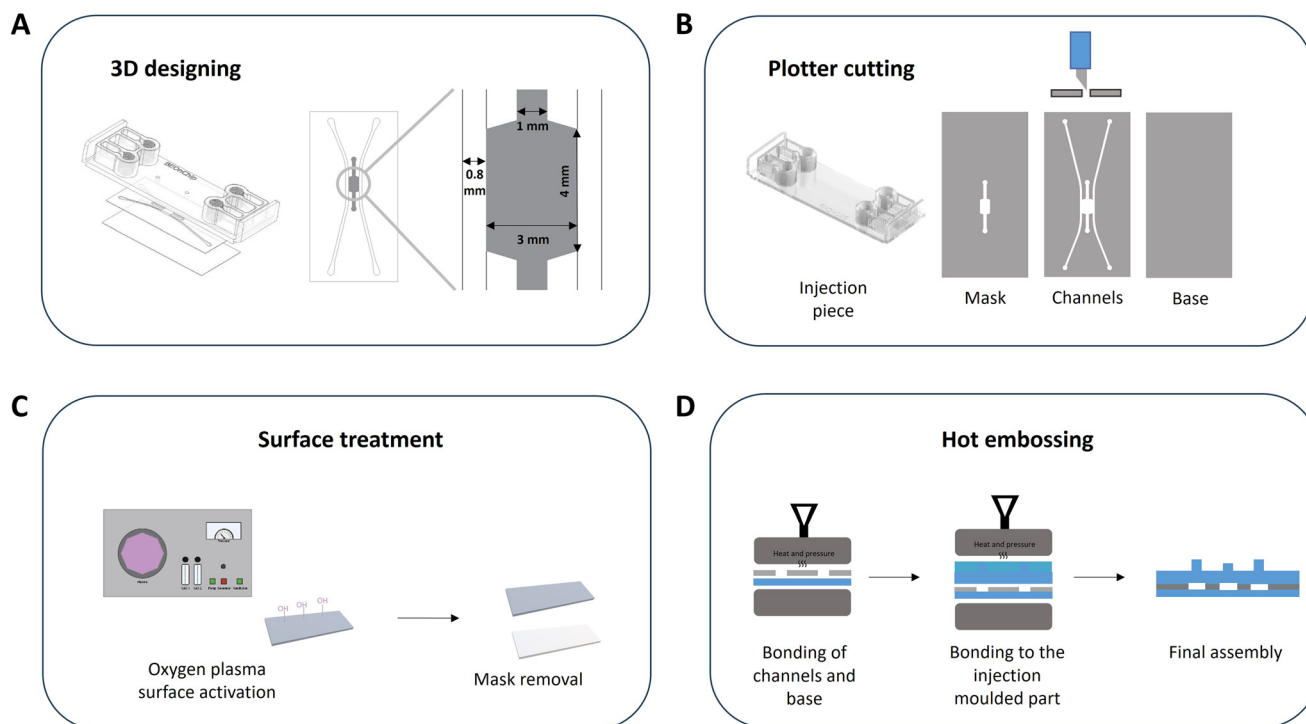
Fig. 1 Fabrication process. (A) Design of the device. 3D exploded model and 2D channel layer with details of the central chamber area. (B) Material selection and cutting. The device is made of olefin copolymers and plotter cutting is used to achieve the desired geometries. The design of the central channel is used to obtain the mask and the central and lateral channels. (C) Surface treatment. Oxygen plasma surface activation process using the mask with the central chamber geometry. (D) Thermocompression bonding. Firstly, the channel layer is bonded to the base; finally, channels are bonded to the injection piece.

chamber were measured in 10 devices. Measurements of the mask and the final device were made with the magnifying lens after the cutting and fabrication processes. Three measurements were made in each area tested in each of the masks, that is, three in the central chamber and three in the central channel. The same process was performed for each of the final devices. The software used to make these measurements is Image Acquisition and Measurement Software IC Measure. Measurements of the seeded device were made by introducing a collagen hydrogel with fluorescent microspheres into the central chamber of the device and observing the chip under the confocal microscope. The same measurement process was used: 3 were made in each relevant area, the central channel width and the chamber width. On the other hand, the height of the channel was also measured, as fluorescence allows it. Nikon EZ-C1 FreeViewer and Fiji software were used for these measurements. Both the gel creation process and the seeding process are explained in the following section (Fig. 2).

2.2 Design and validation of different geometries

Four different geometries, which were called "guitar", "waves", "diamond" and "hammer", were designed using AutoCAD, and the manufacturing protocol explained above was then followed. With these designs, and apart from demonstrating the effectiveness of the surface treatment in

achieving different geometries, the flow velocities, pressure, and shear stresses on the walls along the different sections of each device were obtained using CFD, as explained in section 2.4. Fig. S1E† shows both the mask and the channels of the device for the four designs.

To validate these geometries, a collagen gel (collagen type I, rat tail Corning, 354249) containing green FluoSpheres (FluoSpheres, Invitrogen, F8811) was introduced in the central chamber to observe its confinement and perfused with rhodamine (Rhodamine B, Sigma-Aldrich, R6626) in PBS through the side channels, as explained in section 2.3.

2.3 Collagen gel preparation and seeding

First, the hydrogel mixture was prepared according to the required collagen concentration (4 mg mL^{-1}). In this case, 50 µL of gel mixture was prepared by mixing the reagents in the following order: 0.61 µL of distilled water, 5 µL of 5× DMEM (Sigma-Aldrich, D5523), 0.47 µL of 1N NaOH (Sigma-Aldrich, 221465), 18.92 µL of 10.57 mg mL^{-1} collagen (collagen type I, rat tail Corning, 354249), and finally, 25 µL of medium DMEM (Sigma-Aldrich, D5523). 1 µL of green FluoSpheres (Invitrogen, F8811) was added to the mixture for visualization. The hydrogel was kept on ice during preparation to avoid polymerization, and a volume of 7 to 10 µL was seeded depending on the geometry of the device. After seeding, the devices were placed into an incubator (37
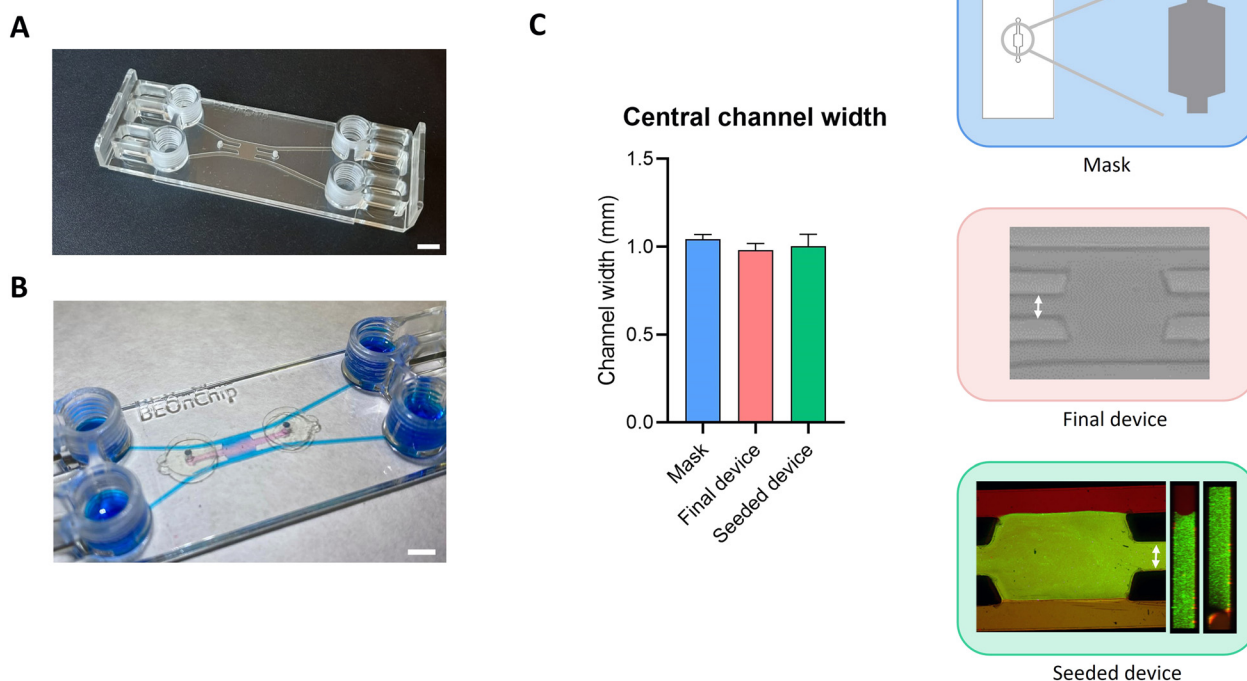
Fig. 2 Gradient device. (A) Final device. Scale bar: 4 mm. (B) Seeded final device. Collagen gel (4 mg ml^{-1}) through the central channel and PBS with blue food coloring through the lateral channels. Scale bar: 4 mm. (C) The graph shows measurements of the central channel (mask, final device and seeded device). Seeded devices are the devices that are filled with the hydrogel. The side views shown in the image "seeded device" are made along the central channel (channels and camera), thus measuring the height of the device's channels. The mask and final device are measured using a Nikon SMZ745 magnifying lens and seeded devices using a Nikon Eclipse Ti confocal microscope.

°C and 5% CO_2) for 15 minutes to polymerize, turning them every 5 minutes to achieve a homogeneous distribution of FluoSpheres. The seeding process of the device is shown in Fig. S2.†

The fluid flow experiments were done using a syringe pump (NE-1000 Multi-PhaserTM) at 5 μL min^{-1} for 30 minutes. The syringes filled with 1 μg mL^{-1} Rhodamine B (Sigma-Aldrich, R6626) in PBS were connected to the chips using PTFE tubes (1/16″ OD × 1/32″ ID, Darwin Microfluidics) and screw connectors (1/4″-28, Elveflow Microfluidics). The solution was perfused to test the confinement of the hydrogel and the diffusion process through the hydrogel.

To evaluate the hydrogel confinement inside the central chamber, the hydrogel distribution was assessed by confocal microscopy.

2.4 Computational simulation

To study the multiphysics transport of oxygen due to diffusion and convection through the designed and manufactured devices, Darcy–Stokes equations coupled with a mass transfer equation were solved by discretizing the equations using a finite element approach implemented in the open-source package FEniCS.[45,46]

The corresponding CAD files were used to extract the geometries of the channels and chamber of each microdevice. In the channels, the Stokes equation was used to simulate the fluid flow under laminar conditions, while the fluid flow in the porous hydrogel that fills the chamber was modeled by means of the Darcy equation. These geometries were then meshed in Gmsh, an open-source finite element mesh generator.[47] On average, around 330 000 elements with an average size of 0.1 mm were used for each device. The fluid was considered with water properties (density $\rho = 1000$ kg m^{-3}, viscosity $\mu = 1$ mPa s) and modeled as a monophasic and incompressible fluid under isothermal and laminar conditions, since the Reynolds number, Re = $Lv\rho\mu^{-1}$ is well below 100. A permeability of $\kappa = 1.78 \times 10^{-8}$ mm^2 was considered for the hydrogel as a porous material.[47] Boundary conditions for fluid flow were defined as a fixed flow of 10^{-5} kg s^{-1} at the inlets, atmospheric pressure (zero pressure) at the outlets, and zero velocity conditions along the channel walls. The oxygen diffusion coefficient throughout the device was considered $D = 3.29 \times 10^{-3}$ mm^2 s^{-1}.[48] Boundary conditions for oxygen were considered fixed at the inlets, with a value of 0.21×10^{-9} mol mm^{-3}, while the initial distribution of oxygen in all the domains was considered homogeneous with a value of 0.189×10^{-9} mol mm^{-3}. Darcy–Stokes equations were solved in a steady state, while the mass transfer equation for oxygen was solved time-dependently. The velocity field obtained from the fluid flow in the channels and the chamber was used in the convection term of the oxygen transfer. The simulation time for mass transfer was 2 minutes as oxygen reaches steady state during

this period based on the simulation conditions in this study and the changes after this time are negligible, aligning with the objectives of our study. All geometries were then analyzed under the same conditions, and the distributions of shear stress and oxygen concentration were computed as described in the Results and discussion section.

2.5 Blood–brain barrier-on-a-chip

Regarding the cell culture, human brain vascular pericytes and human hippocampal astrocytes (Sciencell, #1200 and #1830, respectively) were cultured in T-75 culture flasks coated with poly-L-lysine (2 µg cm^{-2} in sterile water) (Sciencell, #0413) in their respective growth media. A pericyte medium kit (PM, Sciencell, #1201) or an astrocyte medium kit (AM, Sciencell, CA, #1801) was supplemented with 1% v/v pericyte or astrocyte growth supplement, respectively: 10% v/v fetal bovine serum (FBS) and 1% v/v penicillin/streptomycin. The human brain endothelial cell line (hCMEC/D3, Merck-Millipore, SCC066) was cultured in T-75 culture flasks coated with collagen type I from rat tail (25 µg mL^{-1} in phosphate buffered saline (PBS)) (Sigma-Aldrich, C3867-1VL) in an EndoGRO™ MV cell medium kit (Merck Life Science, SCME004) supplemented with bFGF (1 ng mL^{-1}) (Merck-Millipore, F3685). The cells were maintained in a humidified incubator (37 °C and 5% CO_2) and the medium was replaced every 2 days. For further experiments, the cells were used until passage 5.

2.5.1 BBB assembly in the microfluidic device. To conduct the BBB assembly, on day 1, astrocytes and pericytes in the fibrin hydrogel used as a 3D scaffold were injected into the central chamber. On day 3, hCMEC/D3 cells were attached to one of the lateral channels coated with collagen type I from rat tail. Astrocytes and pericytes were detached with 0.05% of trypsin/EDTA (Sciencell, #0183) and a mixture of 25 000 of each cell type was prepared and centrifuged at 1000g for 5 minutes. Meanwhile, a filtered solution of fibrinogen (3 mg mL^{-1} in PBS) (Sigma-Aldrich, F8630-16) and thrombin (100 UI in PBS) (Sigma-Aldrich, T4648) was maintained on ice. Then, the cell pellet was gently resuspended in 50 µL fibrinogen solution, and 1 µL of 125 mM $CaCl_2$ (final concentration 2.5 mM) and 1 µL of thrombin (final concentration 2 UI) were added and rapidly mixed and injected gently into the central chamber. The chip was immediately flipped upwards and downwards every 20 seconds for 3 minutes to assure the homogeneous distribution of cells in the whole chamber height. Then, the chip was incubated for 25 minutes at 37 °C and 5% CO_2 to promote hydrogel polymerization. After that time, the central chamber inlets were sealed with adhesive. Finally, the lateral fluidic channels were perfused with a mixture of astrocytes and ENDOGRO® medium in a ratio of 1:1 with all the supplements at the concentration needed for all cell types (BBB medium). Evaporation reservoirs were filled with PBS and the devices were maintained at 37 °C and 5% CO_2. After 48 hours, the endothelial barrier assembly was performed in one of the lateral channels previously coated

with a collagen solution (25 µg mL^{-1} in PBS) for 50 minutes to promote the cell attachment. Meanwhile, hCMEC/D3 cells were detached with 0.25% trypsin/EDTA (ThermoFisher Scientific, #25200056) and 150 000 cells were centrifuged at 1000g for 5 minutes and resuspended in 50 µL of BBB medium and immediately included in the collagen-coated channel. At this moment, the chip was left in a vertical position allowing the endothelial cells to make contact with the hydrogel wall by gravity for 2 hours at 37 °C and 5% CO_2. The cell medium was changed every day until day 7, and bright-field microscopy images were taken on day 7 using an inverted optical microscope (Nikon Ti2 microscope).

Cell viability was also determined on day 7 using calcein-AM (ThermoFisher, C3100MP) to stain alive cells and ethidium homodimer-1 (EthD-1) (ThermoFisher, L3224B) for dead cells. A live/dead solution was prepared following the manufacturer's instructions, obtaining a solution with a final concentration of 2 µM calcein AM and 4 µM EthD-1 in PBS. The cells were incubated with the live/dead solution for 1 hour at room temperature and washed carefully with PBS twice. The cells in PBS were observed using an inverted fluorescence microscope (Olympus IX7).

2.5.2 Immunofluorescence. To determine the proper development of the BBB in the fabricated device, characteristic proteins of the TJs between endothelial cells, zonula occludens (ZO-1) and VE-cadherin, were labelled by immunofluorescence. The BBB assembled on day 7 was washed with PBS and fixed with commercial formalin solution (4% w/v formaldehyde, Sigma-Aldrich, HT5011) for 15 min at room temperature. The fixed cells were rinsed three times with glycine solution (1.5 mg mL^{-1} in PBS) and permeabilized with 0.1% TritonX-100 in glycine solution for 10 min at RT. After that, the cells were washed three times with 0.1% TritonX-100 in PBS (PBS-T) and blocked with 3% bovine serum albumin (BSA, Sigma-Aldrich, A3059) in PBS-T for 1 hour at RT. Primary antibodies against ZO-1 (0.5 mg mL^{-1}, 1:100, ThermoFisher Scientific, 33-9100) and VE-cadherin (1 mg mL^{-1}, 1:100, Abcam, ab33168) in 3% BSA in PBS-T were added and incubated overnight at 4 °C. Then, the cells were washed three times with PBS and incubated with fluorophore-conjugated secondary antibodies anti-rabbit Alexa 568 (2 mg mL^{-1}, 1:1000, ThermoFisher Scientific, A-11036) and anti-mouse Alexa 488 (1:1000, ThermoFisher Scientific, A-10667) in 1% BSA in PBS-T for 2 hours at RT. Afterwards, the cells were incubated with Hoechst 33342 (1:1000, Invitrogen, H3570) for 15 min at RT. Finally, the cells were washed three times with PBS and the BBB was observed by confocal microscopy at 63× (Leica TCS SP5 Multi-photon system).

2.5.3 Permeability assay. To evaluate the permeability through the assembled BBB, standard fluorescent tracers with different molecular weights were injected into the endothelial channel on day 7. Sterilized solutions of 100 µM sodium fluorescein (NaFl, 376 Da, Sigma-Aldrich, F6377) and FITC-dextran 70 (Dextran 70, 7000 Da; Sigma-Aldrich, 90718) prepared in BBB medium were employed for the permeability assays. On day 7, the cells were washed with PBS to remove cell debris, and after that, NaFl or Dextran 70 was injected

into the endothelial channel, and the BBB medium was added to the non-endothelial channel. Then, images were captured using both bright field and fluorescence settings with an inverted fluorescence microscope (Nikon Eclipse Ti2). Measurements were carried out in triplicate and permeability coefficients (P) were determined as detailed by Campisi and collaborators:[49]

$$P = \left(\frac{1}{(\text{ICht1} - \text{ITt1})} \right) \times \left(\frac{(\text{ITt2} - \text{ITt1})}{(\Delta t)} \right) \times \frac{\text{VT}}{A} \quad \text{cm s}^{-1}$$

where ICht1 and ITt1 are the fluorescence intensity at the initial time in the endothelial channel and the central chamber, respectively (u.a.), ITt2 is the intensity in the central chamber at the final time (u.a.), Δt is the difference between the initial and the final time (s), VT is the volume of the central chamber (cm^3), and A is the surface area of the endothelial wall (cm^2).

2.6 Statistics and image analysis

All data are represented as the mean value ± standard deviation. A Mann–Whitney non-parametric test was performed to analyze the differences in cell death over time (biocompatibility test). Matlab (The MathWorks, Inc) and GraphPad Prism 8® software (GraphPad Software Inc, USA) were used for this purpose. Note that a p-value of less than 0.05 was found to be statistically significant and a value greater than 0.05 was found to be non-significant. The permeability assays were analyzed employing the unpaired statistical T-test using the GraphPad Prism 8® software (GraphPad Software Inc, USA). All microscopy images related to the cell culture were processed using ImageJ/Fiji ® software (NIH, USA).

3. Results and discussion

3.1 Manufacturing of the microfluidic device

The fabrication technique developed in this study demonstrates that biomimetic models with a large contact area between the cavities of the fabricated microfluidic device can be achieved. This is achieved thanks to the applied surface treatment, which confines the hydrogel in the required area. We can also demonstrate that it is possible to fabricate different designs such as those shown in Fig. 3, while any other geometry can be produced. In this way, a closer simulation of the human system can be achieved as cells would be exposed to controlled shear stress distribution along the same channel, also permitting direct contact between the different cell types.

To validate this fabrication process, the reproducibility of the devices was studied. For that, measurements of the central channel were made throughout the manufacturing process using a magnifying lens and a confocal microscope. These measurements were taken on 10 devices from the same batch; thus, all fabrication processes were carried out on the same day. Firstly, the mask was measured, secondly the newly manufactured final device was measured, and finally the device seeded with collagen was measured. Regarding the
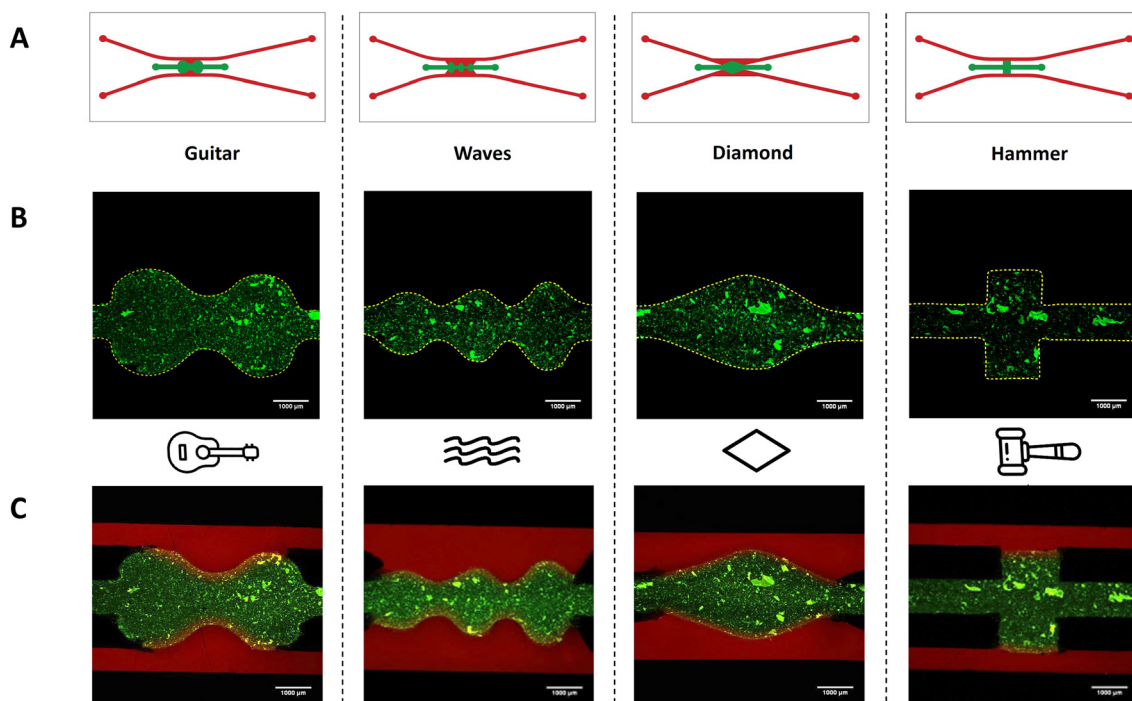

Fig. 3 Patterns of the central chamber: guitar, waves, diamond, and hammer. (A) The final model of the 4 geometries designed using AutoCAD. (B) Confocal microscopy images of the hydrogel confinement in the final devices with four different geometries. (C) Flow validation in the devices by perfusing a rhodamine solution through the side channels. Scale bar 1000 μm.

central channel width, the measurements of the mask (1.04 ± 0.02 mm), the final device (0.98 ± 0.03 mm) and the seeded final device (1 ± 0.07 mm) were similar, and no significant differences were observed (Fig. 2). A similar result was obtained regarding the central chamber width; for the mask, the mean of the measurements was 3.11 ± 0.03 mm, for the final device, 2.94 ± 0.05 mm and for the seeded final device, 2.99 ± 0.13 mm (Fig. S3†). In relation to the height of the channels, the practical average was 196.56 ± 2.72 μm compared to the theoretical value of 200 μm, so no significant differences were noted (Fig. S3†). These results showed that the manufacturing process was carried out efficiently, and this methodology presents high reproducibility.

3.2 Customizable hydrogel patterns in pillarless microfluidic devices

An added value of this treatment is the fact that it is possible to reproduce complex geometries using a simpler manufacturing method than photopatterning[40,43] with the ability to create a variety of designs, and, what's more, with total channel-to-channel contact that the phaseguide technique[38,39] containing a step does not give. With this surface treatment, it is possible to design more precise geometries that simulate more realistic tissues or histological structures, reproducing not only the shape but also the shear

forces under flow conditions. Shear stress is very important when simulating body parts *in vitro*, as demonstrated in many studies. Several physiological functions, such as vascular tone and integrity, and regulation of homeostasis are controlled by mechanical forces acting on the arterial wall as shear stresses. There is also sufficient evidence on the role of shear stresses in homeostasis and the evolution of vascular disease.[50,51]

In this work, four different geometries that could be related to histological structures were fabricated. For example, it might be possible to simulate blood vessels under physiological or pathological conditions using the "guitar" and "diamond" patterns, which have similar shear stresses to capillaries and venules. Another example of close simulation is the intestinal villi, thanks to the "wave" design. In all cases, the same manufacturing process was used since there is no *a priori* limitation to obtain the desired geometry.

As with the original pattern, the confinement of the collagen gel into these devices was assessed. The results showed perfect confinement of the gel under static and flow conditions and diffusion over time for the proposed different designs (Fig. 3).

The distributions of fluid shear stresses and oxygen concentration obtained in finite element analysis using FEniCS are shown in Fig. 4 and 5. In Fig. 4, we examine the impact of pillars within the "gradient" chip on both shear stress distribution and oxygen concentration. The presence of pillars
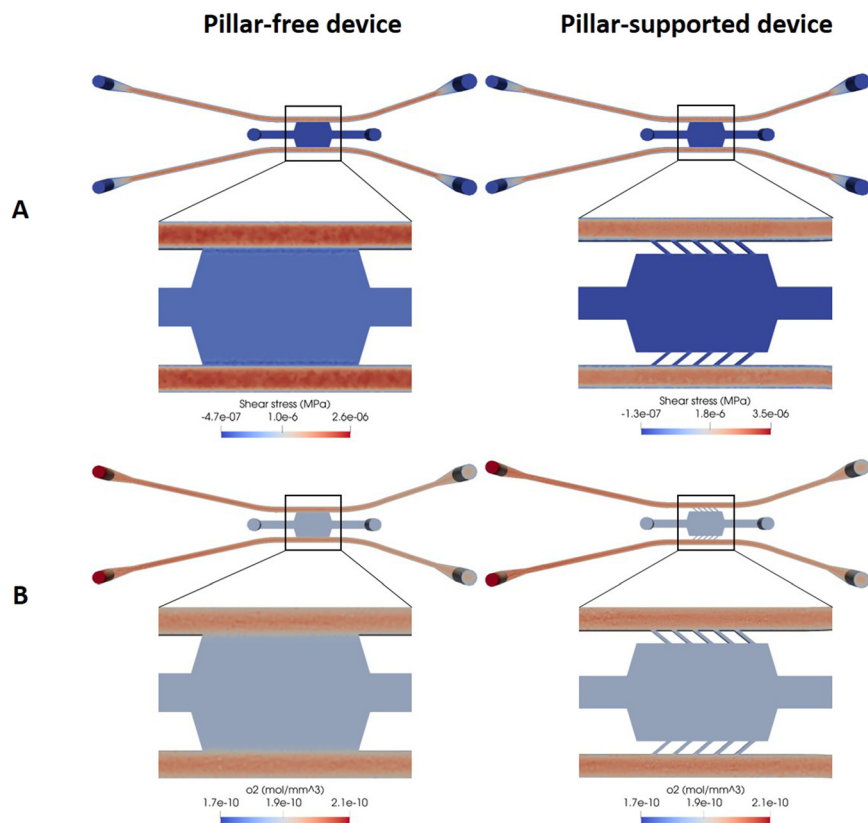

Fig. 4 Computational simulation of the gradient designs: pillar-free and pillar-supported. (A) Shear stress profile in MPa. (B) Oxygen concentration along the device in mol mm⁻³.
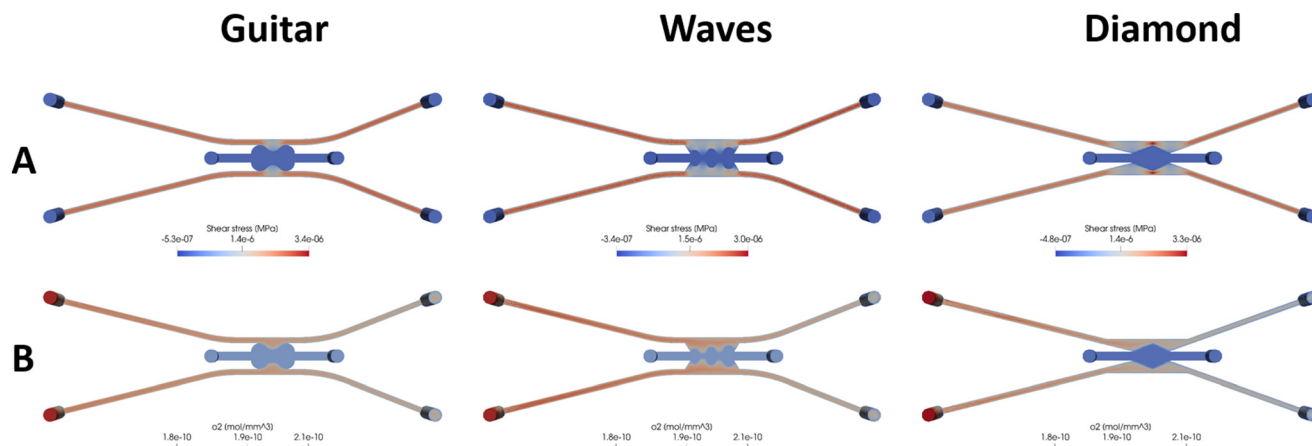
Fig. 5 Computational simulation of the devices of the designs guitar, waves and diamond. (A) Shear stress profiles in MPa. (B) Oxygen concentration in mol mm^{-3}.

hinders fluid flow, resulting in reduced shear stress within the chamber. Conversely, in the abutment-free design, the channel–chamber interface exhibits higher shear stress and oxygen concentration. If we study all abutment-free models (Fig. 4 and 5), the shear stress along the channels was around 3.5 Pa, decreasing in regions close to the chamber. The "gradient" device shows the lowest shear stress in comparison with the other models. The geometry of this chip in inlets and outlets is different from the other models, and the boundary areas in this model are slightly greater than in the others. Also, the width of this model is bigger than the rest. All these differences in geometry cause the difference in shear stress, pressure drop, and velocity in this model compared to the others. The "hammer" and "gradient" devices were characterized by almost constant shear stress and velocity along the lateral channels (around 3.4 Pa and 2.6 Pa for shear stress and 70 mm s^{-1} and 120 mm s^{-1} for velocity, respectively). In these designs, without any section change in the channels, the value of the velocity and, consequently, the shear stress was constant along the channels.

Fig. S4† shows the velocity magnitude profile in a cross-section view of the devices. Like the shear stress, the velocity in the channel in the regions close to the chamber decreased compared to the velocity along the channels far from the chamber in all the models. Maximum velocity can be observed in the channels for all the models except for the "diamond", which occurs in the regions close to the chamber and is about 160 mm s^{-1}. In this model, at that region, the area of the channels is reduced and causes an increase in the velocity magnitude. In particular, the lowest velocity in the regions close to the chamber occurred in the "guitar" and "wave" shapes (approx. 65 mm s^{-1} and 60 mm s^{-1}, respectively) (Fig. 5A). Concerning the "diamond" geometry, the velocity in the lateral channels was lower than in the other geometries (around 120 mm s^{-1}), decreasing to 60 mm s^{-1} close to the chamber area. In the zone close to the central chamber, the velocity was lower in regions with wider areas and higher in the peaks (160 mm s^{-1} in the red area). In

Fig. 4B and 5B, the oxygen concentration can be seen for the different designs. Oxygen diffuses and moves due to fluid flow convection. The simulation results show that it reaches a steady state quickly. As can be seen in these figures, the oxygen concentration is reduced in the chamber region due to the low fluid velocity in this region for all the designs.

In contrast, due to the ease of movement of fluid, there are substantial concentrations of oxygen in the channels. The maximum oxygen concentration is in the inlets, as can be expected, and is reduced along the channel. The "wave" design shows a better distribution of oxygen in the chamber in comparison with the other designs. Obviously, in all the designs, the oxygen concentration in the interface between channels and the chamber is higher than in the other regions of the chamber. For the pressure results (Fig. S4†), in all the geometries, the pressure drop between inlets and outlets was around 10^{-3} MPa.

The choice of the chip design depends on the purpose and goals of the research. Considerations such as ease and cost-effectiveness of fabrication, versatility for various applications, and the ability to mimic the *in vivo* environment of the cells and tissues under study, or to examine physiological or pathological processes, should be considered.[52]

The simulation results from this study indicate that the "gradient" design has the lowest shear stress distribution among the options, while the "diamond" design shows a higher amount of shear stress. If lower shear stress is required, as in the case of intestinal epithelial cells, the "gradient" design can be a suitable choice. Conversely, in situations where shear stress is important, such as for vascular endothelial cells to maintain the physiological function of blood vessels or metastatic cancer cells that move in tissues where higher shear stress is needed, the "diamond" design may be the better option.[53]

Clearly, the obtained computational simulation data provide relevant information about the shear stresses and behavior of the fluid inside the device. Therefore,

computational simulation for the study of fluid dynamics in devices, together with the fact that tuneable hydrogel patterns can be generated, emerges as a powerful tool for OOC technology. Thus, by combining both tools, more biomimetic microdevices can be achieved, which allows going one step further in the development of more realistic *in vitro* models. Here, we have demonstrated that through this fabrication technique, we can achieve devices where cells can be subjected to different shear stresses along the channel as can happen in blood vessels or in the intestine.[54–56] It also highlights the value computing the oxygen concentration at every point of the device which permits the oxygen gradients in the chamber to be controlled and optimized, as happens in different locations in the human body.

3.3 Hydrogel confinement and fluid flow validation

To validate the microfluidic device, the hydrogel confinement under static and flow conditions was assessed. Both cell-free and cell-confined (Fig. S5†) collagen gel seeding was performed to evaluate the confinement in the central chamber. Furthermore, the device was connected to the flow to observe the maintenance of confinement and diffusion through the central chamber.

Under static conditions, the confocal microscopy images showed that the hydrogel maintained its shape and height over time (7 days), denoting the good confinement of the central chamber and high cell viability (Fig. S5†). A similar validation was performed under flow conditions. After seeding the devices with a collagen gel

containing green FluoSpheres (central channel) and perfusing PBS with rhodamine (lateral channels), the hydrogel remained confined over time, and a process of diffusion through the gel was observed (Fig. 6). Here, the small size of rhodamine-B particles (10 μm) contributes to rapid diffusion within a short duration (as illustrated in Fig. 6, notable diffusion occurs every 5 minutes from 5 to 25 minutes).

The evidence presented has shown that the applied treatment allows confining the hydrogels within the central chamber (without pillars) over time and retaining them even under flow conditions. Coupled with this, diffusion with a continuous profile not disrupted by pillars has been observed inside the central chamber, generating gradients inside the device. Both parameters, diffusion and gradients, are critical in the development of 3D experimental models, so this device can be used to test the diffusion process or gradient formation related to the study of cellular metabolism (nutrients, oxygen…) or drug diffusion.

Finally, this device has been seeded with different hydrogels other than collagen, such as fibrin (shown below) and PLMA100 (data not shown). The result was the same: confinement of the hydrogel in the central chamber.

3.4 BBB-assembly in the pillarless microfluidic device

To further validate the pillarless device, we developed a BBB model consisting of human astrocytes and pericytes embedded in the fibrin hydrogel confined into the central chamber with a continuous endothelial barrier in a lateral
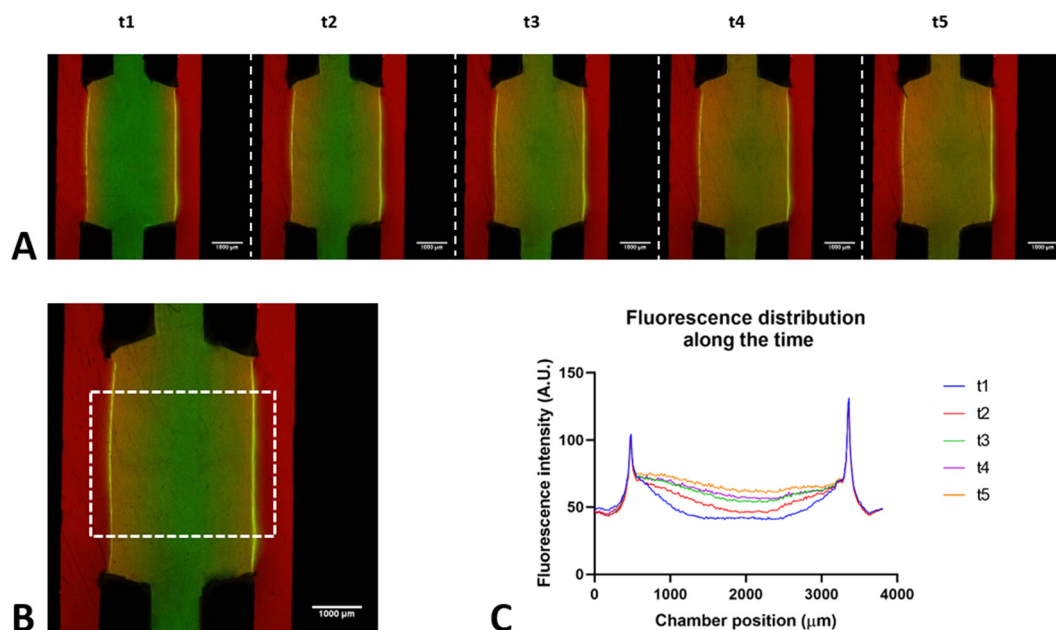

Fig. 6 Evaluation of the confinement of the hydrogel in the central chamber and diffusion in the microfluidic device. (A) Microscopy images show the diffusion process from the lateral channels to the central chamber from t_1 = 5 min to t_5 =25 min. Scale bar 1000 μm. (B) Fluorescence study area. (C) Fluorescence with time in the marked area. It could be seen that the fluorescence increases with increasing time. In other words, the rhodamine progresses through the central chamber.
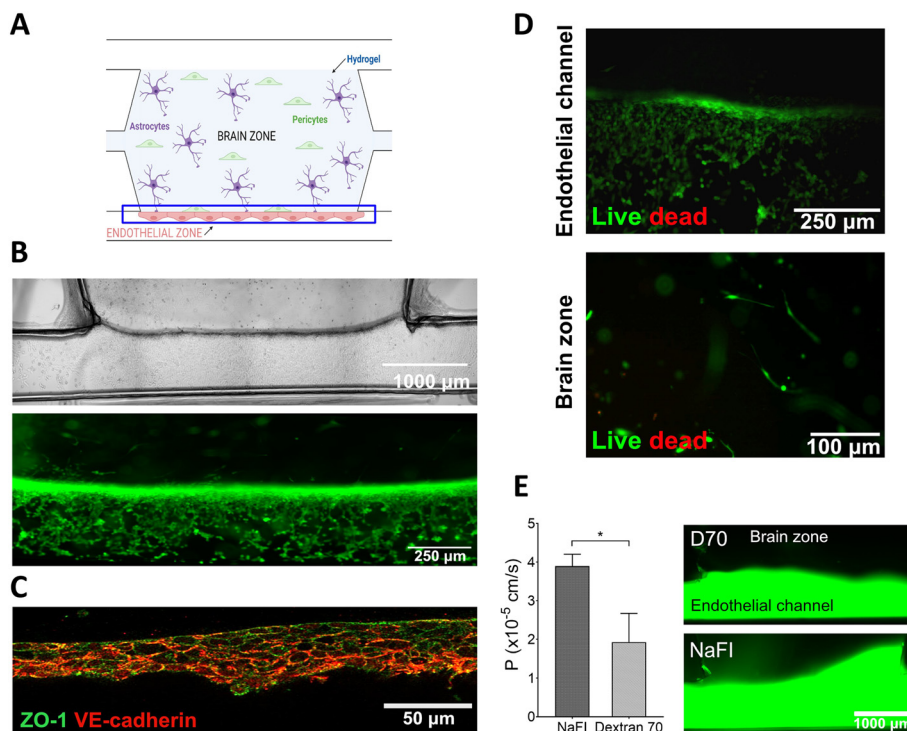
Fig. 7 BBB-assembly in the microfluidic device. (A) Schematic representation of the neurovascular cell arrangement in the microdevice. (B) Bright-field and fluorescence images of the BBB with a live cell marker. Scale 1000 μm and 250 μm, respectively. (C) Immunofluorescence of specific markers for tight junctions between endothelial cells hCMEC/D3. Scale bar 50 μm. (D) Cell viability assay in the endothelial and brain zone on day 7. Scale bar 250 μm and 100 μm, respectively. (E) Permeability coefficient values and end-time fluorescence images of permeability assays with standard tracers (NaFl and Dextran 70). Scale bar 1000 μm.

channel (Fig. 7A). Fibrin is a hydrogel that is widely regarded as an ideal 3D matrix for applications related to the CNS. It has already been approved by the Food and Drug Administration (FDA) and is highly biocompatible with impressive mechanical properties, making it suitable for use in neuronal transplantation.[57] Fig. 7B shows optical bright field images that reveal the localization of hCMEC/D3 endothelial cells in the lateral channel, as well as their accumulation at the well-defined interface between the hydrogel and the channel. This positioning allows for close contact with the pericytes and astrocytes, closely mimicking the natural BBB. In addition, Fig. 7B shows, labelled in green, the alive cells which form the uninterrupted BBB on the wall of the confined hydrogel. Besides, tight junctions (TJs) between endothelial cells are crucial for the BBB's ability to prevent the passage of molecules into the CNS. To evaluate the development of the assembled BBB, ZO-1 and VE-cadherin were immunostained. Fig. 7C shows clear evidence of the presence of ZO-1 stained in green and VE-cadherin stained in red, mainly expressed between adjacent endothelial cells.

Meanwhile, a live/dead assay was performed to assess cell viability within the fabricated microdevice. The green signal from the endothelial cells indicated a nearly 100% survival rate until the seven-day period. Additionally, the hydrogel zone exhibited mostly viable cells. As a result, both the fibrin hydrogel and the fabricated microdevice demonstrated

biocompatibility with neurovascular cultures such as human astrocytes, pericytes, and endothelial cells (Fig. 7D).

Finally, permeability assays were conducted using fluorescent tracers with different molecular weights. On day 7, NaFl (376 Da) and D70 (70 000 Da) were injected into the endothelial channel to evaluate the BBB's permeability performance (Fig. 7E) and fluorescence images were captured in the neuronal area. As Fig. 7E displays, the results obtained from the BBB-on-a-chip indicated size-dependent exclusion, where smaller molecules (NaFl: 3.90×10^{-5} cm s^{-1}) passed through the BBB faster than larger ones (Dextran 70: 1.92×10^{-5} cm s^{-1}). The permeability values obtained from our developed BBB were consistent with previous reports in the literature for microfabricated 3D models.[58]

In summary, an uninterrupted endothelial barrier was established which emulates the neurovascular network of the brain. Immunofluorescence images demonstrated the development of TJs between adjacent endothelial cells which are crucial for maintaining the restricted BBB permeability. Furthermore, permeability assays confirmed the ability of the assembled BBB to exclude molecules based on size, with permeability coefficient values consistent with those previously reported for microfabricated 3D models. Therefore, the results obtained confirm the potential of our pillarless microdevice for a functional 3D BBB model that could be used to evaluate potential therapies for CNS diseases.

4. Conclusions

In this work, a new microfluidic platform without pillars has been developed to allow direct contact between cells, eliminate inert materials and recreate more biomimetic models. The evidence presented in this work has shown that the new fabrication technique allows recreation of different geometries mimicking tissue structures and generation of specific shear stress profiles to obtain more accurate experimental models. Furthermore, the results demonstrated that the treatment allows confinement of the hydrogels over time even under flow conditions. With this reproducible fabrication, the devices can recreate uniform gradients within the central chamber thanks to the absence of the pillars, thus generating a continuous diffusion process through the hydrogel. Finally, pillarless microfluidic devices have been biologically validated with the generation of a BBB, so the described technology meets the necessary requirements for the development of *in vitro* 3D organ-on-a-chip models.

Author contributions

COR: conceptualization, formal analysis, investigation, methodology, visualization, writing – original draft, writing – review & editing. SPF, TR, CB, and MA: formal analysis, investigation, methodology, visualization, writing – review & editing. AL, MM and JS: conceptualization, funding acquisition, project administration, supervision, writing – review & editing. MD, IO, RM and SO: conceptualization, funding acquisition, project administration, supervision, writing – review & editing.

Conflicts of interest

I. Ochoa, M. Doblaré, R. Monge and S. Oliván are promoters and consultants for BeOnChip S.L.

Acknowledgements

References

1 J. S. Kochhar, S. Y. Chan, P. S. Ong, W. G. Lee and L. Kang, *Microfluidic devices for drug discovery and analysis*, Woodhead Publishing Limited, 2013.

2 F. S. Pasqualini, M. Y. Emmert, K. K. Parker and S. P. Hoerstrup, Organ Chips: Quality Assurance Systems in Regenerative Medicine, *Clin. Pharmacol. Ther.*, 2017, **101**(1), 31–34, DOI: **10.1002/cpt.527**.

3 A. G. Monteduro, S. Rizzato, G. Caragnano, A. Trapani, G. Giannelli and G. Maruccio, Organs-on-chips technologies – A guide from disease models to opportunities for drug development, *Biosens. Bioelectron.*, 2023, **231**(March), 115271, DOI: **10.1016/j.bios.2023.115271**.

4 Y. Zhao, E. Y. Wang, F. B. L. Lai, K. Cheung and M. Radisic, Organs-on-a-chip: a union of tissue engineering and microfabrication, *Trends Biotechnol.*, 2023, **41**(3), 410–424, DOI: **10.1016/j.tibtech.2022.12.018**.

5 S. N. Bhatia and D. E. Ingber, Microfluidic organs-on-chips, *Nat. Biotechnol.*, 2014, **32**(8), 760–772, DOI: **10.1038/nbt.2989**.

6 D. E. Ingber, Human organs-on-chips for disease modelling, drug development and personalized medicine, *Nat. Rev. Genet.*, 2022, **23**(8), 467–491, DOI: **10.1038/s41576-022-00466-9**.

7 S. Cho, S. Lee and S. I. Ahn, Design and engineering of organ-on-a-chip, *Biomed. Eng. Lett.*, 2023, **13**(2), 97–109, DOI: **10.1007/s13534-022-00258-4**.

8 A. Sood, A. Kumar, V. K. Gupta, C. M. Kim and S. S. Han, Translational Nanomedicines Across Human Reproductive Organs Modeling on Microfluidic Chips: State-of-the-Art and Future Prospects, *ACS Biomater. Sci. Eng.*, 2023, **9**(1), 62–84, DOI: **10.1021/acsbiomaterials.2c01080**.

9 T. M. Keenan and A. Folch, Biomolecular gradients in cell culture systems, *Lab Chip*, 2007, **8**(1), 34–57, DOI: **10.1039/b711887b**.

10 R. H. W. Funk, Ion Gradients in Tissue and Organ Biology, *Biol. Syst.: Open Access*, 2013, **2**(1), DOI: **10.4172/2329-6577.1000105**.

11 R. N. Pittman, Oxygen gradients in the microcirculation, *Acta Physiol.*, 2011, **202**(3), 311–322, DOI: **10.1111/j.1748-1716.2010.02232.x**.

12 A. S. Popel, Theory of Oxygen Transport to Tissue, *Crit. Rev. Biomed. Eng.*, 1989, **17**(3), 257–321.

13 V. Corradi, *et al.*, Lipid-Protein Interactions Are Unique Fingerprints for Membrane Proteins, *ACS Cent. Sci.*, 2018, **4**(6), 709–717, DOI: **10.1021/acscentsci.8b00143**.

14 L. Chen, *et al.*, Inflammatory responses and inflammation-associated diseases in organs, *Onco Targets Ther*, 2018, **9**(6), 7204–7218, [Online], Available: **https://www.impactjournals.com/oncotarget/**.

15 K. Kohli, V. G. Pillarisetty and T. S. Kim, Key chemokines direct migration of immune cells in solid tumors, *Cancer Gene Ther.*, 2022, **29**(1), 10–21, DOI: **10.1038/s41417-021-00303-x**.

16 C. T. Taylor and S. P. Colgan, Regulation of immunity and inflammation by hypoxia in immunological niches, *Nat. Rev. Immunol.*, 2017, **17**(12), 774–785, DOI: **10.1038/nri.2017.103**.

17 S. SenGupta, C. A. Parent and J. E. Bear, The principles of directed cell migration, *Nat. Rev. Mol. Cell Biol.*, 2021, **22**(8), 529–547, DOI: **10.1038/s41580-021-00366-6**.

18 J. S. Dutton, S. S. Hinman, R. Kim, Y. Wang and N. L. Allbritton, Primary Cell-Derived Intestinal Models: Recapitulating Physiology, *Trends Biotechnol.*, 2019, **37**(7), 744–760, DOI: **10.1016/j.tibtech.2018.12.001**.

19 Y. Wang, *et al.*, Formation of Human Colonic Crypt Array by Application of Chemical Gradients Across a Shaped Epithelial Monolayer, *Cell. Mol. Gastroenterol. Hepatol.*, 2018, **5**(2), 113–130, DOI: **10.1016/j.jcmgh.2017.10.007**.

20 C. Li, Z. Shi, J. B. Holman, B. Qiu and D. Weiping, On-chip modeling of tumor evolution: Advances, challenges and opportunities, *Mater. Today Bio*, 2023, **21**, DOI: **10.1016/j.mtbio.2023.100724**.

21 J. M. Ayuso, *et al.*, Tumor-on-A-chip: A microfluidic model to study cell response to environmental gradients, *Lab Chip*, 2019, **19**(20), 3461–3471, DOI: **10.1039/c9lc00270g**.

22 F. Wang, The signaling mechanisms underlying cell polarity and chemotaxis, *Cold Spring Harbor Perspect. Biol.*, 2009, **1**(4), 1–16, DOI: **10.1101/cshperspect.a002980**.

23 C. W. Chang, *et al.*, A polydimethylsiloxane-polycarbonate hybrid microfluidic device capable of generating perpendicular chemical and oxygen gradients for cell culture studies, *Lab Chip*, 2014, **14**(19), 3762–3772, DOI: **10.1039/c4lc00732h**.

24 S. H. Oh, C. L. Ward, A. Atala, J. J. Yoo and B. S. Harrison, Oxygen generating scaffolds for enhancing engineered tissue survival, *Biomaterials*, 2009, **30**(5), 757–762, DOI: **10.1016/j.biomaterials.2008.09.065**.

25 S. Kim, H. J. Kim and N. L. Jeon, Biological applications of microfluidic gradient devices, *Integr. Biol.*, 2010, **2**(11–12), 584–603, DOI: **10.1039/c0ib00055h**.

26 Y. Wang, T. Mukherjee and Q. Lin, Systematic modeling of microfluidic concentration gradient generators, *J. Micromech. Microeng.*, 2006, **16**(10), 2128–2137, DOI: **10.1088/0960-1317/16/10/029**.

27 M. Tehrani-Rokh, A. Z. Kouzani and J. R. Kanwar, Gradient generating microfluidic devices for cell cultivation, *Procedia Eng.*, 2012, **29**, 1740–1744, DOI: **10.1016/j.proeng.2012.01.205**.

28 J. S. Liu, *et al.*, Design and Validation of a Microfluidic Chip with Micropillar Arrays for Three-dimensional Cell Culture, *Fenxi Huaxue*, 2017, **45**(8), 1109–1114, DOI: **10.1016/S1872-2040(17)61029-6**.

29 H. Uwamori, T. Higuchi, K. Arai and R. Sudo, Integration of neurogenesis and angiogenesis models for constructing a neurovascular tissue, *Sci. Rep.*, 2017, **7**(1), 1–11, DOI: **10.1038/s41598-017-17411-0**.

30 M. Polinkovsky, E. Gutierrez, A. Levchenko and A. Groisman, Fine temporal control of the medium gas content and acidity and on-chip generation of series of oxygen concentrations for cell cultures, *Lab Chip*, 2009, **9**(8), 1073–1084, DOI: **10.1039/b816191g**.

31 M. Virumbrales-Muñoz, *et al.*, Enabling cell recovery from 3D cell culture microfluidic devices for tumour microenvironment biomarker profiling, *Sci. Rep.*, 2019, **9**(1), 1–14, DOI: **10.1038/s41598-019-42529-8**.

32 S. R. Li, *et al.*, Glucose absorption drives cystogenesis in a human organoid-on-chip model of polycystic kidney disease, *Nat. Commun.*, 2022, **13**(1), 7918, DOI: **10.1038/s41467-022-35537-2**.

33 H. Gholizadeh, *et al.*, In vitro interactions of aerosol formulations with human nasal epithelium using real-time monitoring of drug transport in a nasal mucosa-on-a-chip, *Biosens. Bioelectron.*, 2023, **223**, 115010, DOI: **10.1016/j.bios.2022.115010**.

34 J. Loessberg-Zahl, J. Beumer, A. van den Berg, J. C. T. Eijkel and A. D. van der Meer, Patterning biological gels for 3d cell culture inside microfluidic devices by local surface modification through laminar flow patterning, *Micromachines*, 2020, **11**(12), 1–11, DOI: **10.3390/mi11121112**.

35 V. Palacio-Castañeda, L. Kooijman, B. Venzac, W. P. R. Verdurmen and S. Le Gac, Metabolic switching of tumor cells under hypoxic conditions in a tumor-on-a-chip model, *Micromachines*, 2020, **11**(4), 1–13, DOI: **10.3390/MI11040382**.

36 K. M. Denecke, *et al.*, Microfluidic Model to Evaluate Astrocyte Activation in Penumbral Region following Ischemic Stroke, *Cells*, 2022, **11**(15), 1–14, DOI: **10.3390/cells11152356**.

37 N. R. Wevers, *et al.*, A perfused human blood-brain barrier on-a-chip for high-throughput assessment of barrier function and antibody transport, *Fluids Barriers CNS*, 2018, **15**(1), 1–12, DOI: **10.1186/s12987-018-0108-3**.

38 K. M. Bircsak, *et al.*, A 3D microfluidic liver model for high throughput compound toxicity screening in the OrganoPlate®, *Toxicology*, 2021, **450**(January), 152667, DOI: **10.1016/j.tox.2020.152667**.

39 H. Ehlers, *et al.*, Vascular inflammation on a chip: A scalable platform for trans-endothelial electrical resistance and immune cell migration, *Front. Immunol.*, 2023, **14**(January), 1–11, DOI: **10.3389/fimmu.2023.1118624**.

40 M. Nikolaev, *et al.*, Homeostatic mini-intestines through scaffold-guided organoid morphogenesis, *Nature*, 2020, **585**(7826), 574–578, DOI: **10.1038/s41586-020-2724-8**.

41 G. A. Primo and A. Mata, 3D Patterning within Hydrogels for the Recreation of Functional Biological Environments, *Adv. Funct. Mater.*, 2021, **31**(16), 2009574, DOI: **10.1002/adfm.202009574**.

42 N. Gjorevski, *et al.*, Tissue geometry drives deterministic organoid patterning, *Science*, 2022, **375**(6576), eaaw9021, DOI: **10.1126/science.aaw9021**.

43 A. Mora-Boza, A. Mulero-Russe, N. Di Caprio, J. A. Burdick, A. Singh and A. J. García, Facile Photopatterning of Perfusable Microchannels in Synthetic Hydrogels to Recreate Microphysiological Environments, *Adv. Mater.*, 2023, **35**(52), 1–13, DOI: **10.1002/adma.202306765**.

44 Y. Zhao, *et al.*, Recent advances in drug delivery systems for targeting brain tumors, *Drug Delivery*, 2023, **30**(1), 1–18, DOI: **10.1080/10717544.2022.2154409**.

45 M. S. Alnaes, *et al.*, The FEniCS Project Version 1.5, *Archive of Numerical Software*, 2015, vol. 3(100), pp. 9–23, DOI: **10.11588/ans.2015.100.20553**.

46 A. Logg, G. Wells and K.-A. Mardal, Automated solution of differential equations by the finite element method, *The FEniCS Book*, 2011, vol. 84.

47 C. Geuzaine and J. Remacle, Gmsh: A 3-D finite element mesh generator with built-in pre- and post-processing facilities, *Int. J. Numer. Methods Eng.*, 2009, **79**, 1309–1331, DOI: **10.1002/nme.2579**.

48 G. Santos Rosalem, *Desenvolvimento de uma nova plataforma Organ-on-a-Chip para a biomimetização do microambiente da medula óssea*, Universidade Federal de Minas Gerais, Escola de Engenharia, 2022.

49 M. Campisi, Y. Shin, T. Osaki, C. Hajal, V. Chiono and R. D. Kamm, 3D self-organized microvascular model of the human blood-brain barrier with endothelial cells, pericytes and astrocytes, *Biomaterials*, 2018, **180**, 117–129, DOI: **10.1016/j.biomaterials.2018.07.014**.

50 B. Zhang, J. Gu, M. Qian, L. Niu, H. Zhou and D. Ghista, Correlation between quantitative analysis of wall shear stress and intima-media thickness in atherosclerosis development in carotid arteries, *Biomed. Eng. Online*, 2017, **16**(1), 1–17, DOI: **10.1186/s12938-017-0425-9**.

51 P. F. Davies, Hemodynamic shear stress and the endothelium in cardiovascular pathophysiology, *Nat. Clin. Pract. Cardiovasc. Med.*, 2009, **6**(1), 16–26, DOI: **10.1038/ncpcardio1397**.

52 A. C. Urbaczek, *et al.*, Endothelial Cell Culture Under Perfusion On A Polyester-Toner Microfluidic Device, *Sci. Rep.*, 2017, **7**(1), 1–12, DOI: **10.1038/s41598-017-11043-0**.

53 J. A. Espina, M. H. Cordeiro, M. Milivojevic, I. Pajić-Lijaković and E. H. Barriga, Response of cells and tissues to shear stress, *J. Cell Sci.*, 2023, **136**(18), 1–11, DOI: **10.1242/jcs.260985**.

54 L. C. Delon, *et al.*, A systematic investigation of the effect of the fluid shear stress on Caco-2 cells towards the optimization of epithelial organ-on-chip models, *Biomaterials*, 2019, **225**(December 2018), 119521, DOI: **10.1016/j.biomaterials.2019.119521**.

55 E. Roux, P. Bougaran, P. Dufourcq and T. Couffinhal, Fluid Shear Stress Sensing by the Endothelial Layer, *Front. Physiol.*, 2020, **11**(July), 1–17, DOI: **10.3389/fphys.2020.00861**.

56 C. Souilhol, *et al.*, Endothelial responses to shear stress in atherosclerosis: a novel role for developmental genes, *Nat. Rev. Cardiol.*, 2020, **17**(1), 52–63, DOI: **10.1038/s41569-019-0239-5**.

57 P. Lu, *et al.*, Long-distance growth and connectivity of neural stem cells after severe spinal cord injury, *Cell*, 2012, **150**(6), 1264–1273, DOI: **10.1016/j.cell.2012.08.020**.

58 D. C. Fernandes, R. L. Reis and J. M. Oliveira, Advances in 3D neural, vascular and neurovascular models for drug testing and regenerative medicine, *Drug Discovery Today*, 2021, **26**(3), 754–768, DOI: **10.1016/j.drudis.2020.11.009**.